Check for updates

Received: 13 March 2023 | Accepted: 13 April 2023

DOI: 10.1002/jemt.24332

RESEARCH ARTICLE

MICROSCOPY RESEARCH & TECHNIQUE WILEY

Fast autofocus method for piezoelectric microscopy system for high interaction scenes

Xiaopeng Hao | Bowen Zhong | Zhan Liao | Lining Sun

The College of Mechanical and Electrical Engineering, Soochow University, Suzhou, China

Correspondence
Bowen Zhong, The College of Mechanical and Electrical Engineering, Soochow University, Suzhou 215000, China.
Email: zhbw@suda.edu.cn

Funding information
National Natural Science Foundation of China, Grant/Award Number: 52175541

Review Editor: Alberto Diaspro

Abstract

Piezoelectric objective driver positioners are increasingly used in the field of microscopy. They have the advantages of high dynamic and fast response. This paper presents a fast autofocus algorithm for highly interactive microscope system. First, the Tenengrad gradient of the down-sampled image is used to calculate the image sharpness, and Brent search method is adopted to quickly converge to the correct focal length. At the same time, the input shaping method is used to eliminate the displacement vibration of the piezoelectric objective lens driver and further accelerate the image acquisition speed. Experimental results show that the proposed scheme can improve the speed of the automatic focusing task of the piezoelectric objective driver and improve the real-time focus of the automatic microscopic system.

Highlights

- A high real-time autofocus strategy.
- A vibration control method suitable for a piezoelectric objective driver.

KEYWORDS
autofocus, input shaping, microscope, piezo objective driver

1 | INTRODUCTION

A crucial part of the procedure for diagnosing and screening serious diseases is microscopic inspection. The diagnostician repeatedly moves the carrier stage of the microscope to see each local region of the tissue sample during illness diagnosis to observe the cellular properties of the lesion and precisely evaluate the reason. Additionally, because the surface of the pathology sample is not flat (Montalto et al., 2011), it frequently falls out of focus when viewed through a high magnification microscope, requiring the examiner to correct the focus manually and repeatedly. The number of sample sections from patients that the pathology department must process each day makes the doctors' work highly demanding. Literature studies and in-person encounters have shown that pathology diagnosticians experience psychiatric disorders, cervical spondylosis, and dizziness at a considerably higher rate than the general population.

The highly interactive real-time automatic microscope system can relieve the operator of a lot of repetitive work, reducing workload and the risk of occupational diseases. It automatically focuses as the operator moves the sample position and provides the examiner with clear images in real time through the CCD camera. This places very high demands on the autofocusing algorithm's speed to accommodate the diagnostician's habit of using the microscope and to deliver good images in real time. An autofocus speed of about 100 milliseconds can provide diagnosticians with a favorable experience when current digital focusing technology is combined with the usage habits of visiting medical practitioners.

The piezoelectric objective driver is a scientific instrument that uses the piezoelectric effect to convert electrical energy into mechanical energy to adjust the distance between the objective and the biological sample, offering the advantage of fast response and high precision. It is widely used in the fields of autofocus, digital whole slide imaging (WSI) (Bian et al., 2020) and image z-stack scanning. However, this mechanical structure is prone to vibration, which limits its performance. Feedback-based PID control (Gu et al., 2014) are still widely used for vibration control, but the PID method requires the

 © 2023 Wiley Periodicals LLC.

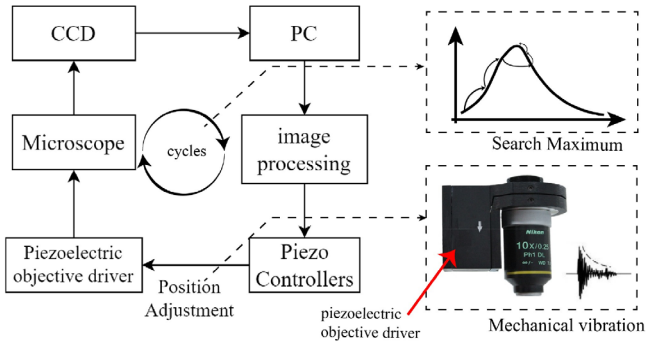

FIGURE 1 System architecture.

integration of complex position sensing devices and long adjustment times.

Passive focusing based on image processing is the main focusing method of automatic microscope system (Chen et al., 2010). The passive focus method uses a sharpness evaluation function to measure the sharpness information of the image and uses a search algorithm to adjust the focus without the need for an external sensing device. Sun (Sun et al., 2004) made a comprehensive comparative study of 18 kinds of evaluation functions, and gave a series of evaluation performance indicators. Hu (Zhong et al., 2019) compared the performance of eight evaluation functions, and used RFT function and SMD2 function multiplication as the image evaluation method, combined with the adaptive window pickup method to achieve a good focusing effect. However, the current autofocus algorithm faces the problem of slow speed and cannot meet the usage scenarios with high requirements for interactivity.

In conclusion, there are two issues with the current concentrating method of high interaction that need to be resolved. First, slow search and lengthy image processing are issues with automatic focusing algorithms based on passive focus. Second, the shooting speed is further impacted by the piezoelectric objective driver's output vibration. In this study, the grayscale center of gravity approach, the Brent search method, and the Tenengrad gradient value of the down sampled image are coupled to increase the computational speed of the focusing strategy. The system vibration issue can be managed and the focusing speed is further enhanced using the input shaping technique.

The rest of the paper is structured as follows: Section 2 introduces the experimental system; Section 3 describes the autofocus method; Section 4 describes the input shaper damping method; Section 5 describes the experiments; and Section 6 provides conclusions.

2 | SYSTEM INTRODUCTION AND MAIN QUESTIONS

Figure 1 shows the main workflow of the piezoelectric automatic microscope system. The experimental system is mainly composed of optical microscope, CCD camera, piezoelectric objective driver, and the piezo controllers.

TABLE 1 Parameters of the piezoelectric objective lens driver.

Piezoelectric objective lens driver			
Stroke	**Resolution**	**Repeatability**	**Max. load**
60 (μm)	6 (nm)	<60 (nm)	1 (kg)

The piezoelectric controller receives the signal from the PC software and drives the piezoelectric objective driver to adjust the focal length by changing the voltage. Then, the piezoelectric objective driver receives commands from the piezoelectric controller and drives the objective lens to adjust the focus. The control software in PC was developed using Visual Studio 2022 and can perform tasks such as image acquisition, platform movement, and autofocus. The parameters of the piezoelectric objective driver are shown in Table 1. The performance parameters can meet the experimental requirements. Our research focuses on two aspects to improve the focusing speed, on the one hand, we can improve the search algorithm to improve efficiency and reduce the number of cycles, and on the other hand, we can save time by reducing the mechanical vibration caused by each movement of the lens.

3 | AUTOFOCUS STRATEGY

3.1 | Image sharpness evaluation function

The key technologies of autofocus for the microscopic systems are evaluation function selection and Maximal searching algorithm. To obtain the image sharpness value, the image is first converted into a grayscale image. To further speed up the calculation of sharpness, we use the image down sampling method to reduce the image data size. In the process of image acquisition, there is inevitably noise information, and after experiments, we found that the median filtering algorithm can better handle the noise information of the image (Figure 2).

Scholars have proposed a range of assessment methods to calculate image sharpness based on the fact that the intensity of adjacent pixels in a clear image changes substantially. Unbiasedness, single peak, real-time, and generality (Sha et al., 2017) must all be met by the ideal sharpness evaluation function. To select the best evaluation function, we tested the performance of the commonly used articulation evaluation functions, including SMD, Brenner, Laplace, Energy, Tenengrad, and Variance. A total of 72 images from the left and right sides of the focal plane were collected. The sharpness curve was calculated by using the above evaluation functions. The normalized results by *Z*-score method were shown in Figure 3. Meanwhile, Figure 3 shows the difference of sharpness curves calculated by evaluation function before and after image preprocessing.

10970029, 2023, 7, Downloaded from https://analyticalsciencejournals.onlinelibrary.wiley.com/doi/10.1002/jemt.24332 by Tsinghua University Library, Wiley Online Library on [08/06/2024]. See the Terms and Conditions (https://onlinelibrary.wiley.com/terms-and-conditions) on Wiley Online Library for rules of use; OA articles are governed by the applicable Creative Commons License

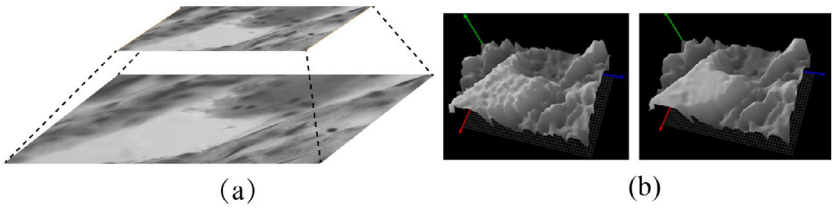

FIGURE 2 Image preprocessing (a) down sampling and (b) median filtering.

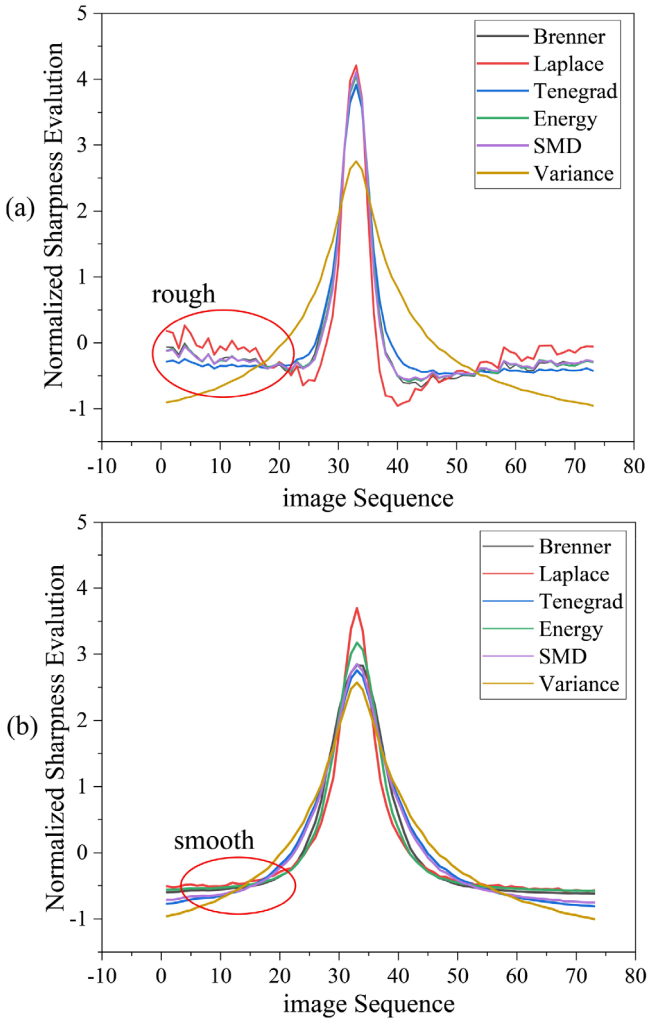

FIGURE 3 Comparison of the arithmetic speed of six evaluation functions (a) no preprocessing and (b) preprocessing.

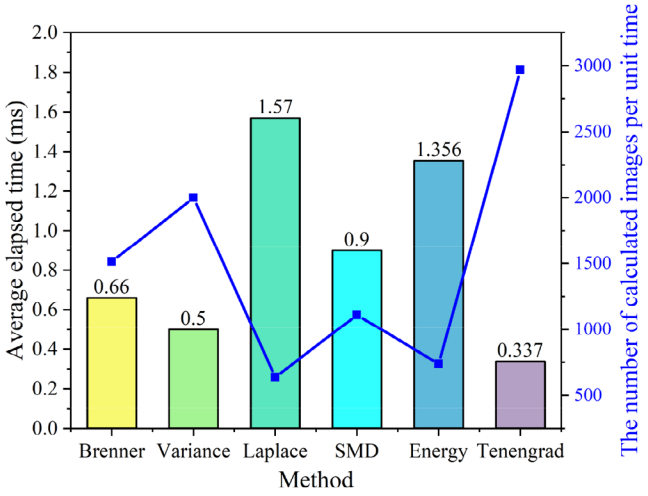

FIGURE 4 Comparison of the effects of six evaluation functions.

The image preprocessing suggested in this paper might further improve the quality of the evaluation function, as shown in Figure 3. Furthermore, every evaluation function satisfies the standards for determining image sharpness. We also looked into the computational efficiency of the six evaluation functions, as shown in Figure 4.

From Figure 4, the Tenengrad method has the fastest computation speed, which can compute nearly 3000 images of 960p per second. Therefore, we choose the Tenengrad function (Tenenbaum, 1971) to calculate the image sharpness, which uses the Sobel operator to extract the gradient values in the horizontal and vertical directions of the grayscale image and uses the sum of squares as the image sharpness. The formula is as follows:

$$f = \sum_x \sum_y G(x,y)^2$$

where the expression of $G(x,y)$ is:

$$\begin{aligned} G(x,y) &= \sqrt{\left(G_x^2(x,y) + G_y^2(x,y)\right)} \\ G_x(x,y) &= f(x,y) \otimes T_x \quad G_y(x,y) = f(x,y) \otimes T_y \end{aligned}$$

The operator $\otimes$ represents the convolution operation, the gradient operators T_x and T_y are:

$$T_x = \begin{bmatrix} -1 & -2 & -1 \\ 0 & 0 & 0 \\ 1 & 2 & 1 \end{bmatrix} T_y = \begin{bmatrix} -1 & 0 & 1 \\ -2 & 0 & 2 \\ -1 & 0 & 1 \end{bmatrix}$$

3.2 | Region of interest selection

The focus evaluation functions of the majority of the observed objects satisfy single peak after reasonable image preprocessing, but in a few rare instances, the deformation issue during the production of biological samples can result in the phenomenon of local peaks in the evaluation function, which is unfavorable for the ensuing search for the focus location. We select the area surrounding the grayscale center of the image as the site of ROI since it is typically the area with the maximum information density. To improve the single-peak nature of the evaluation function and to also save computational work (Gu et al., 2015), the sharpness curve of ROI is computed using the

10970029, 2023, 7, Downloaded from https://analyticalsciencejournals.onlinelibrary.wiley.com/doi/10.1002/jemt.24332 by Tsinghua University Library, Wiley Online Library on [08/06/2024]. See the Terms and Conditions (https://onlinelibrary.wiley.com/terms-and-conditions) on Wiley Online Library for rules of use; OA articles are governed by the applicable Creative Commons License

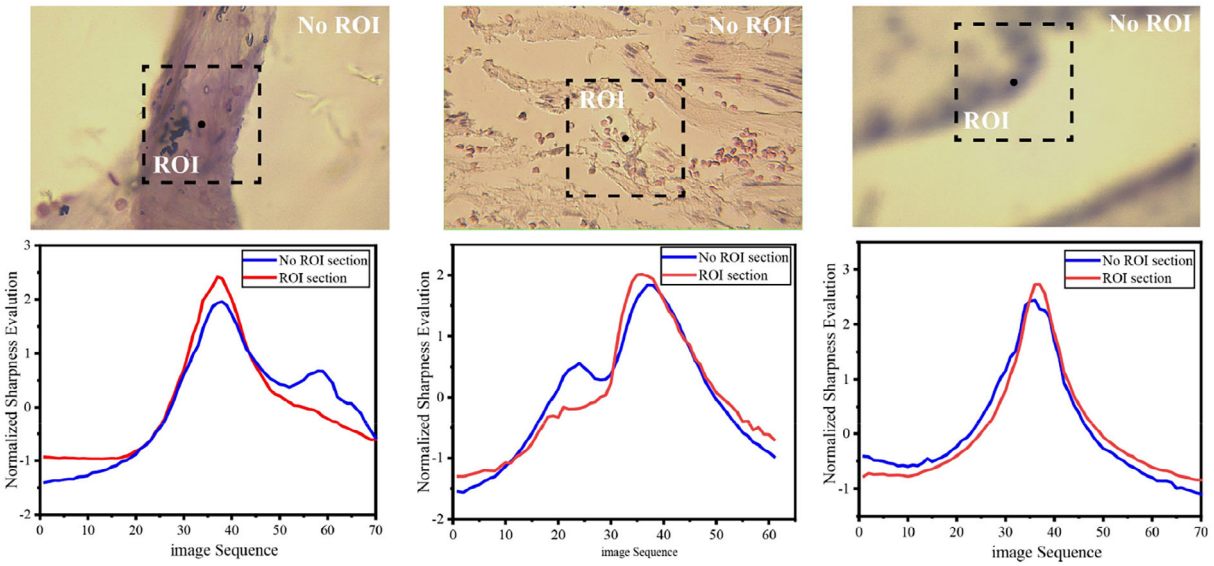

FIGURE 5 Effect of the grayscale gravity method.

evaluation function. The formula for calculating the grayscale center of gravity $(\overline{u},\overline{v})$ is as follows:

$$\overline{u} = \sum_{(u,v)\in\Omega} u\cdot f(u,v) / \sum_{(u,v)\in\Omega} f(u,v)$$
$$\overline{v} = \sum_{(u,v)\in\Omega} v\cdot f(u,v) / \sum_{(u,v)\in\Omega} f(u,v)$$

$f(u,v)$ is the pixel gray value of coordinate (u,v), and Ω is the set of target regions. Figure 5 shows the sharpness curves of three different samples after selecting the ROI using the grayscale gravity method. The effectiveness of the method can be demonstrated by comparing with the original sharpness curves.

3.3 | Brent search

After determining the sharpness function, the autofocus problem is a problem of searching for extreme values.

$$\max_{z\in R} f(z)$$
$$\text{s.t.} \quad z\in[z_{\min}, z_{\max}]$$

where $f(z)$ is the sharpness function and z denotes the travel of the objective lens. The Brent search method requires that the function f(z) be unimodal. The extreme value search method used in this paper is the Brent search method (Brent, 2013), which combines the golden section search method and the parabolic interpolation method to ensure the speed of the search while having a strong robustness. The principle of Brent search algorithm is briefly described below. In the first stage, the Brent search method begins to search using the golden section principle. The idea of golden section search is to shrink the search interval with each iteration. The initial search interval is $[z_{\min}, z_{\max}]$, in which the following formula is: used to determine the two points z_1 and z_2.

$$\begin{cases} z_1 = z_{\min} + (1-\lambda)(z_{\max} - z_{\min}) \\ z_2 = z_{\min} + \lambda(z_{\max} - z_{\min}) \end{cases}$$

where $\lambda = \left(\sqrt{5}-1\right)/2$, λ is called the golden ratio. At this point, the image sharpness values $f(z_1)$ and $f(z_2)$ at z_1 and z_2 are calculated. If $f(z_1) < f(z_2)$, the interval to the left of point z_1 is discarded; otherwise, the interval to the right of point z_2 is discarded, as shown in Figure 6a. This interval maximum can be found by repeating the above operations. But Brent search in order to speed up the search, additional operations are required at this point.

z_3 is determined by $f(z_1)$ and $f(z_2)$, If $f(z_1) < f(z_2) < f(z_3)$ is satisfied, then the next iteration point can be obtained by using parabolic interpolation:

$$z^* = \frac{(z_2^2 - z_3^2)f(z_1) + (z_3^2 - z_1^2)f(z_2) + (z_1^2 - z_2^2)f(z_3)}{2(z_2 - z_3)f(z_1) + (z_3 - z_1)f(z_2) + (z_1 - z_2)f(z_3)}$$

The advantage of parabolic interpolation is that it can converge quickly to the vicinity of the maximum value, as shown in Figure 6b. The next iteration uses z_3, z_2, z^* to continue the search. If the condition is not satisfied, the search continues according to the golden section method. After each iteration, check what kind of search operation can be performed on the iteration condition at this time until the specified search precision is reached.

4 | VIBRATION ELIMINATION

By applying different voltages to the positive and negative electrodes of the PZT material (Gao et al., 2020), the piezoelectric objective

10970029, 2023, 7, Downloaded from https://analyticalsciencejournals.onlinelibrary.wiley.com/doi/10.1002/jemt.24332 by Tsinghua University Library, Wiley Online Library on [08/06/2024]. See the Terms and Conditions (https://onlinelibrary.wiley.com/terms-and-conditions) on Wiley Online Library for rules of use; OA articles are governed by the applicable Creative Commons License

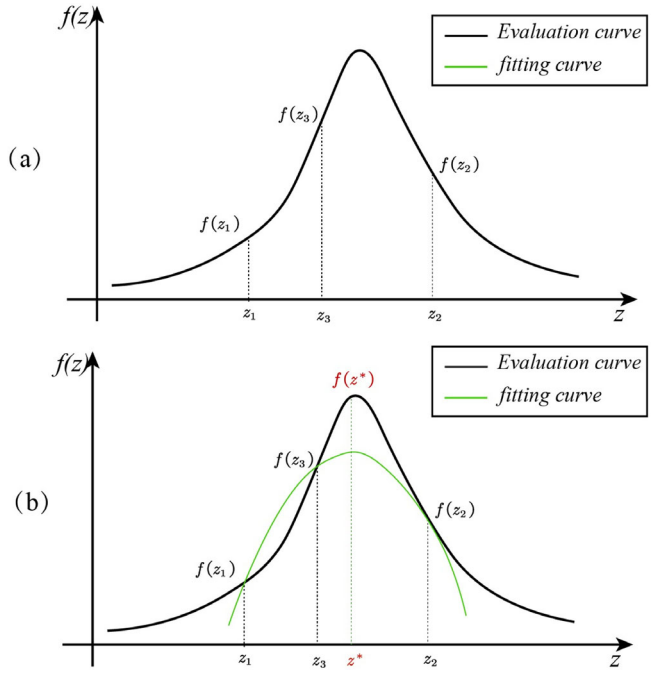

FIGURE 6 Brent search algorithm diagram. (a) Phase I Golden Section and (b) Phase 2 Parabolic interpolation.

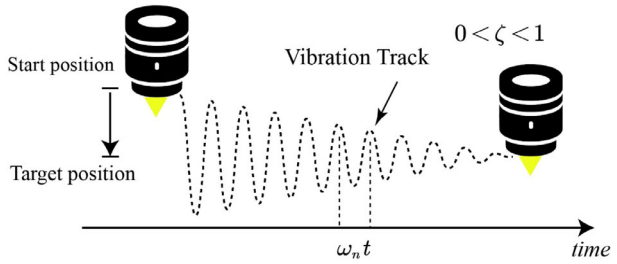

FIGURE 7 Mechanical vibration of the objective lens movement.

driver can be made to move. The output displacement is then amplified by a flexible hinge structure (Chen et al., 2020), with the relationship between the output displacement and the applied voltage magnitude being linear.

Unfortunately, the flexible hinge is a structure with a low damping factor, which generates large residual vibrations after an impact, and it takes some time for the objective to smooth out when it moves to the next designated position, as shown in Figure 7. If the camera starts shooting too early, it will lead to motion blur (Tiwari et al., 2013) of the image, which will have an impact on the subsequent focusing accuracy. The traditional method is to wait for the vibration of the mechanism to end before image acquisition, which will greatly reduce the efficiency of focusing. MIT has suggested the use of input shaping (Bohlke, 1995), a feed-forward control technique, to reduce residual system vibrations. This approach does not call for the addition of sensors or modifications to the device's mechanical design. The damping ratio and the natural frequency are the only two variables needed to

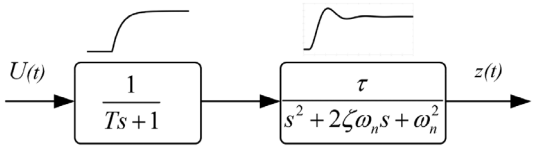

FIGURE 8 System block diagram of piezoelectric objective driver.

create the input shaper. The input shaping approach is frequently employed in devices like cantilever beams because of its benefits.

4.1 | Parameter identification

The transfer function of the system must first be defined in order to determine the two parameters needed for the input shaper. The piezoelectric objective driver can be viewed as a linear system consisting of a first-order inertial link and a second order oscillating system connected in series (Zhong et al., 2011). This is shown in Figure 8.

The displacement transfer function of the piezoelectric objective actuator can be expressed by the following equation:

$$G_z(s) = \frac{1}{Ts+1}\frac{\tau}{s^2+2\zeta\omega_n s+\omega_n^2}$$

where ω_n is the natural frequency of the flexible hinge, ζ is the damping coefficient of the system. We use a displacement sensor to obtain oscillation data when the objective lens moves, and then use the MATLAB System Identification Toolbox to find the transfer function of the system. The results are as follows:

$$G_z(s) = \frac{1.192\times10^9}{s^3+1604s^2+1.894\times10^6 s+2.249\times10^9}$$

After obtaining the transfer function expression, solving the nonlinear equation system can then obtain the damping ratio and natural frequency of the system.

$$\begin{cases} (2\zeta\omega_n T+1)/T = 1604 \\ (\omega_n^2 T+2\zeta\omega_n)/T = 1.894\times10^6 \\ \omega_n^2/T = 2.249\times10^9 \end{cases}$$

The key parameters of the system are calculated $\omega_n = 1269.4, \zeta = 0.1$. The next section briefly describes the design method of the input shaper.

4.2 | Input shaper design

The simplest ZV shaper works as shown in Figure 9. The signal A driving the controlled object is split into two segments, A_1 and A_2. After the action, signal A_1 creates a blue oscillation curve, and signal A_2 is

10970029, 2023, 7, Downloaded from https://analyticalsciencejournals.onlinelibrary.wiley.com/doi/10.1002/jemt.24332 by Tsinghua University Library, Wiley Online Library on [08/06/2024]. See the Terms and Conditions (https://onlinelibrary.wiley.com/terms-and-conditions) on Wiley Online Library for rules of use; OA articles are governed by the applicable Creative Commons License

sent immediately after half a cycle, canceling out each other's vibration.

The ZV shaper design process is as follows, for the second-order oscillation:

$$G(s)=\frac{\omega_n^2}{s^2+2\zeta\omega_n s+\omega_n^2}$$

To eliminate the oscillation of the system after 2 pulses, We need to make the sum of the total impulse response to 0, and in order for the system to reach the target location, we need to set $A_1+A_2=1$. To sum up, the parameters of the ZV shaper can be obtained through the following equations:

$$\begin{cases} A_1+A_2e^{-\zeta\omega_n t_2}\cos(\omega_d t_2)=0 \\ A_2e^{-\zeta\omega_n t_2}\sin(\omega_d t_2)=0 \\ A_1+A_2=1 \\ A_i>0, i=1,2 \end{cases}$$

where $\omega_d=\omega_n\sqrt{1-\zeta^2}$ is the damped frequency. Defining $K=e^{\frac{-\zeta\pi}{\sqrt{1-\zeta^2}}}$ The solution is:

$$\begin{bmatrix} t_1 & t_2 \\ A_1 & A_2 \end{bmatrix}=\begin{bmatrix} 0 & \frac{\pi}{\omega_d} \\ \frac{K}{1+K} & \frac{1}{1+K} \end{bmatrix}$$

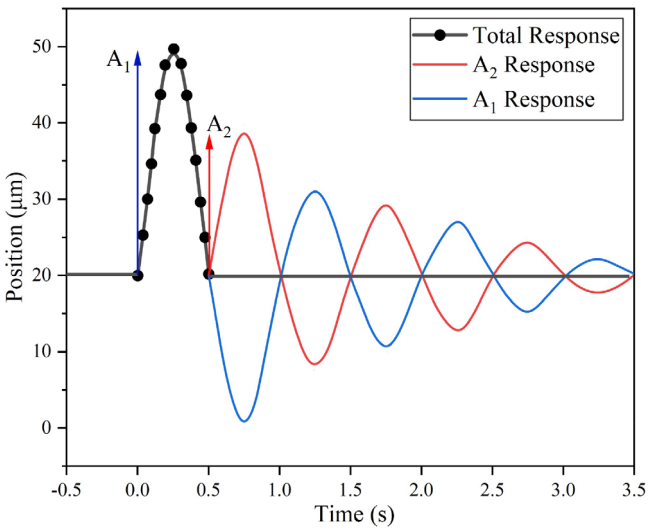

FIGURE 9 Principle of input shaper.

TABLE 2 ZV input shaper parameters.

	Pulse A_1	Pulse A_2
Amplitude	0.5783	0.4217
Delay	0	2487 μs

By substituting the two system parameters calculated in the previous section, the design parameters of the ZV shaper can be obtained (Table 2).

Another ZVD shaper divides the original signal into three pulses, which is more robust to the natural frequency and damping ratio error but will take longer than the ZV shaper due to 1 extra pulse. The calculation result is given directly here:

$$\begin{bmatrix} t_1 & t_2 & t_3 \\ A_1 & A_2 & A_3 \end{bmatrix}=\begin{bmatrix} 0 & \frac{\pi}{\omega_d} & \frac{2\pi}{\omega_d} \\ \frac{K^2}{K^2+2K+1} & \frac{2K}{K^2+2K+1} & \frac{1}{K^2+2K+1} \end{bmatrix}$$

Table 3 shows the design parameters of the ZVD shaper.

The next content will verify the effect of the input shaper on the vibration control of the piezoelectric objective driver. The same voltage is loaded to the piezoelectric objective driver using the uncontrolled, ZV shaper control and ZVD shaper control, respectively, and the vibration is collected using a displacement sensor. The result is shown in Figure 10.

The experimental findings demonstrate that the input shaping method effectively controls the vibration of piezoelectric objective driver. In uncontrolled circumstances, the vibration of objective lens takes 50 ms to stabilize. The objective displacement can stabilize after the feedforward control of ZVD shaper in under 5 ms, allowing the CCD camera to begin acquiring images more quickly. In addition, it is

TABLE 3 ZVD input shaper parameters.

	Pulse A_1	Pulse A_2	Pulse A_3
Amplitude	0.3344	0.4877	0.1778
Delay	0	2487 μs	4974 μs

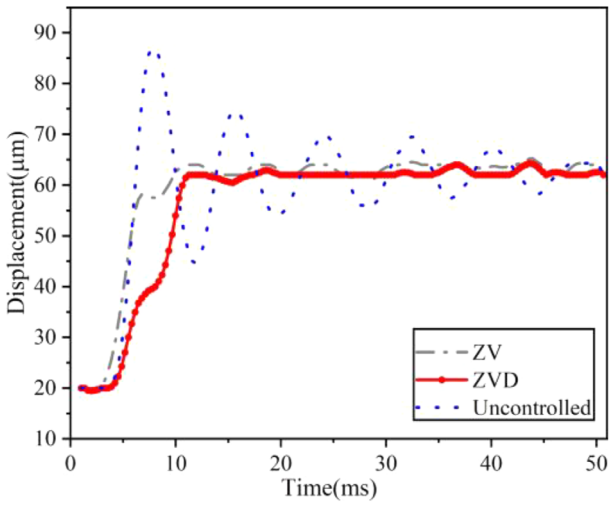

FIGURE 10 Vibration control effect.

10970029, 2023, 7, Downloaded from https://analyticalsciencejournals.onlinelibrary.wiley.com/doi/10.1002/jemt.24332 by Tsinghua University Library, Wiley Online Library on [08/06/2024]. See the Terms and Conditions (https://onlinelibrary.wiley.com/terms-and-conditions) on Wiley Online Library for rules of use; OA articles are governed by the applicable Creative Commons License

evident from the outcomes that ZVD shaper offers superior results over ZV shaper.

5 | EXPERIMENTAL RESULTS

Six frequently used biological samples, including gastrointestinal stromal tumors, breast fibroadenomas, ovarian cystadenomas, nerve cell sections, bone cells, and osteochondromas, were chosen to test the effectiveness of the autofocus algorithm proposed in this paper. The success rate and average elapsed time of the focusing algorithm were tested at 40×, 20×, and 10× objective magnifications, respectively (Figures 11 and 12).

The depth of field (DOF; Xie et al., 2007) is the gap between when the image is clear before and after the objective lens comes into focus. The human eye has a limited capacity for image discrimination. The depth of field increases with decreasing objective lens magnification, making it simpler to correctly focus.

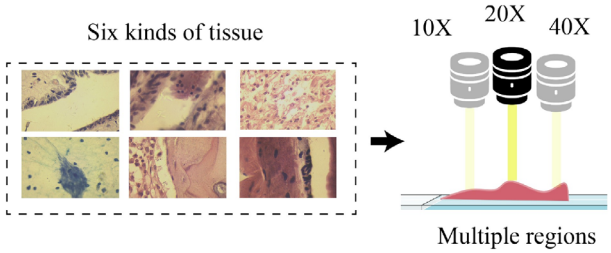

FIGURE 11 Autofocus experiment.

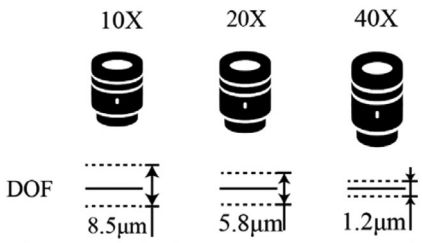

FIGURE 12 The relationship between depth of field and success rate.

The rules to determine whether it is a success are as follows: First, the evaluation function curve of the local position of the current tissue was measured, and the corresponding relationship between the objective lens position and the image sharpness value was obtained. According to the lens depth of field distance, the minimum sharpness value meeting the visual requirements of human eyes was obtained. Then 100 repeated focusing experiments were performed on the location, with the starting position of each focus being random. If the result of the autofocus search is greater than the minimum sharpness value, it is considered a success. The following results show that the autofocus algorithm proposed in this paper has good performance.

The results in Table 3 demonstrate that the ZVD shaper voltage signal driving method in conjunction with the optimized focusing algorithm can regulate the automated focusing time to within 100 ms. The success rate of focusing of six tissue samples remained above 94% at various objective magnifications. At the same time, we contrast the speeds of Brent search, golden section search, and conventional mountain climbing search. When compared to the aforementioned two approaches, Brent search can save between 50 and 100 ms when using the ZVD drive method.

6 | CONCLUSION

This study offers some recommendations for enhancing the interactive microscope system's focusing speed. First, we develop an autofocus strategy that calculates the ROI region of the image using the grayscale center of gravity method, then computes the image sharpness using the Tenengrad gradient function of the down-sampled image, and finally uses the Brent search method, which has a faster convergence speed than other approaches. Second, to increase the focusing speed even more, we employ the ZVD input shaping approach to dampen the piezoelectric objective driver's vibration. After extensive experiments on commonly used biological tissue samples, the experimental results show that the new focusing method can achieve fast focusing in about 100 ms, with a focusing success rate of over 94% at various objective magnifications (Table 4).

AUTHOR CONTRIBUTIONS

Xiaopeng Hao: Software; methodology; conceptualization; investigation; visualization; validation; formal analysis; project administration;

TABLE 4 Autofocus experiment results summary.

Sample name	Average elapsed time (ms)	Success rate		
		10× (%)	20× (%)	40× (%)
Fibroadenoma of breast	98	99.1	96.3	94.6
Cystadenoma of ovary	99	98.2	97.1	95.1
GIST	97	98.5	96.9	95.3
Nerve cell section	99	99.3	97.4	94.8
Osteochondroma	98	98.9	95.6	94.1
Bone cells	101	99.1	96.3	93.9

10970029, 2023, 7, Downloaded from https://analyticalsciencejournals.onlinelibrary.wiley.com/doi/10.1002/jemt.24332 by Tsinghua University Library, Wiley Online Library on [08/06/2024]. See the Terms and Conditions (https://onlinelibrary.wiley.com/terms-and-conditions) on Wiley Online Library for rules of use; OA articles are governed by the applicable Creative Commons License

data curation; writing – review and editing; writing – original draft; resources. **Bowen Zhong:** Methodology; supervision; resources; funding acquisition. **Zhan Liao:** Visualization; writing – original draft. **Lining Sun:** Supervision; writing – original draft.

ACKNOWLEDGMENTS

The work was supported by the National Natural Science Foundation of China (No. 52175541).

FUNDING INFORMATION

The National Natural Science Foundation of China, Grant/Award Number 52175541.

CONFLICT OF INTEREST STATEMENT

The authors declare no conflicts of interest.

DATA AVAILABILITY STATEMENT

Research data are not shared.

REFERENCES

Bian, Z., Guo, C., Jiang, S., Zhu, J., Wang, R., Song, P., Zhang, Z., Hoshino, K., & Zheng, G. (2020). Autofocusing technologies for whole slide imaging and automated microscopy. *Journal of Biophotonics*, *13*(12), e202000227.

Bohlke, K. A. (1995). *Using input shaping to minimize residual vibration in flexible space structures*. PhD thesis, Massachusetts Institute of Technology.

Brent, R. P. (2013). *Algorithms for minimization without derivatives*. Courier Corporation.

Chen, C. Y., Hwang, R. C., & Chen, Y. J. (2010). A passive auto-focus camera control system. *Applied Soft Computing*, *10*(1), 296–303.

Chen, F., Zhang, Q., Gao, Y., & Dong, W. (2020). A review on the flexure-based displacement amplification mechanisms. *IEEE Access*, *8*, 205919–205937.

Gao, X., Yang, J., Wu, J., Xin, X., Li, Z., Yuan, X., Shen, X., & Dong, S. (2020). Piezoelectric actuators and motors: Materials, designs, and applications. *Advanced Materials Technologies*, *5*(1), 1900716.

Gu, C. C., Wu, K. J., Hu, J., Hao, C., & Guan, X. P. (2015). Region sampling for robust and rapid autofocus in microscope. *Microscopy Research and Technique*, *78*(5), 382–390.

Gu, G. Y., Zhu, L. M., Su, C. Y., Ding, H., & Fatikow, S. (2014). Modeling and control of piezo-actuated nanopositioning stages: A survey. *IEEE Transactions on Automation Science and Engineering*, *13*(1), 313–332.

Montalto, M. C., McKay, R. R., & Filkins, R. J. (2011). Autofocus methods of whole slide imaging systems and the introduction of a second-generation independent dual sensor scanning method. *Journal of Pathology Informatics*, *2*(1), 44.

Sha, X., Wang, P., Shan, P., Li, H., & Li, Z. (2017). A fast autofocus sharpness function of microvision system based on the Robert function and gauss fitting. *Microscopy Research and Technique*, *80*(10), 1096–1102.

Sun, Y., Duthaler, S., & Nelson, B. J. (2004). Autofocusing in computer microscopy: Selecting the optimal focus algorithm. *Microscopy Research and Technique*, *65*(3), 139–149.

Tenenbaum, J. M. (1971). *Accommodation in computer vision*. Stanford University.

Tiwari, S., Shukla, V. P., Singh, A., & Biradar, S. (2013). Review of motion blur estimation techniques. *Journal of Image and Graphics*, *1*(4), 176–184.

Xie, H., Rong, W., & Sun, L. (2007). Construction and evaluation of a wavelet-based focus measure for microscopy imaging. *Microscopy Research and Technique*, *70*(11), 987–995.

Zhong, B., Wang, Z., Chen, L., & Sun, L. (2011). Kinetic study of a novel trans-scale precision positioning stage based on stick-slip effect. Proceedings of 2011 international conference on electronic & mechanical engineering and information technology, vol. 1, IEEE, 373–376.

Zhong, B., Zhang, Y., Hu, J., Jin, Z., Wang, Z., & Sun, L. (2019). Improved autofocus method for human red blood cell images. *Applied Optics*, *58*(29), 8031–8038.

How to cite this article: Hao, X., Zhong, B., Liao, Z., & Sun, L. (2023). Fast autofocus method for piezoelectric microscopy system for high interaction scenes. *Microscopy Research and Technique*, *86*(7), 773–780. https://doi.org/10.1002/jemt.24332

10970029, 2023, 7, Downloaded from https://analyticalsciencejournals.onlinelibrary.wiley.com/doi/10.1002/jemt.24332 by Tsinghua University Library, Wiley Online Library on [08/06/2024]. See the Terms and Conditions (https://onlinelibrary.wiley.com/terms-and-conditions) on Wiley Online Library for rules of use; OA articles are governed by the applicable Creative Commons License